International Journal of Greenhouse Gas Control 86 (2019) 201–210

Contents lists available at ScienceDirect

International Journal of Greenhouse Gas Control

journal homepage: www.elsevier.com/locate/ijggc

Salt clogging during supercritical CO_2 injection into a downscaled borehole model

Andreas Berntsen[a], Jelena Todorovic[a], Martin Raphaug[a], Malin Torsæter[a], Elvia Anabela Chavez Panduro[b], Kamila Gawel[a,*]

[a] SINTEF Industry, S. P. Andersens veg 15B, 7031 Trondheim, Norway
[b] Department of Physics, Norwegian University of Science and Technology, Høgskoleringen 5, 7491 Trondheim, Norway

ARTICLE INFO

Keywords:
CO_2 storage
Injectivity
Salt precipitation
Formation damage
Clogging

ABSTRACT

Injection of CO_2 into saline storage aquifers is often accompanied by drying of the formation water and salt precipitation. Subsequent salt clogging of a well bore and the near wellbore rock matrix may lead to injectivity impairment. In this paper we present medium-scale experiments on salt precipitation in the near-well region during a dry CO_2 injection. In an effort to better simulate the geometry and the flow conditions in the field situation our purpose-designed experimental setup enables (1) realistic radial geometry of CO_2 flow, and (2) opened boundary conditions for brine inflow allowing capillary and diffusive flux of brine components from and to practically infinite source of formation water.

During the course of injection, no significant pressure build-up was observed across the rock specimen, indicating that permeable flow paths were not completely clogged. Post-test analysis of the specimen included X-ray computed tomography, powder X-ray diffraction and scanning electron microscopy in order to quantify fluid saturation, brine salinity and halite precipitation. The analysis provided indication of the most probable flow patterns of supercritical CO_2 and CO_2 rich brine in the system. The resulting drying and precipitation is discussed in light of the different drying regimes created under the present flow conditions.

1. Introduction

Storage in subsurface geological formations is one method to mitigate increasing CO_2 concentrations in the atmosphere. In addition to storage capacity and safety, the feasibility of a CO_2 storage project depends on the injectivity – the rate at which CO_2 may be injected into the formation through the injection well. Injectivity is primarily dependent on formation permeability and volume, however, pilot CO_2 storage projects have revealed other factors which may negatively affect injectivity. Among these factors are: presence of bacteria that produce biofilms, or scaling that will plug the formation (Morozova et al., 2011; Zettlitzer et al., 2010) and mineral precipitation due to water evaporation during dry CO_2 injection into saline aquifers (Baumann et al., 2014; Eiken et al., 2011; Grude et al., 2014; Hansen et al., 2013; Martens et al., 2014). Halite (NaCl) precipitation impaired injection at Snøhvit (Eiken et al., 2011; Grude et al., 2014; Hansen et al., 2013) and Ketzin (Baumann et al., 2014; Martens et al., 2014) pilot sites. Halite is the most common deposit as NaCl is the most abundant component in formation waters. The precipitate reduces the porosity and permeability of the formation leading to formation damage and injection impairment. Several physical mechanisms have to be considered in order to adequately model propagation of dry-out front and the extent of salt precipitation (Miri and Hellevang, 2016): (1) displacement of brine by the injected CO_2; (2) evaporation of water into the CO_2 stream which leads to residual brine oversaturation and salt precipitation; (3) back-flow of brine driven by the capillary forces toward the dried out regions; (4) diffusion of salts within the aqueous phase driven by osmotic pressure; (5) enhanced evaporation of water from near interface polycrystalline aggregates due to enhanced surface area – self-enhancing effect (Miri et al., 2015); (6) preferential flow of less dense fluid on the top of a reservoir unit (gravity override).

It has been shown, both in laboratory experiments (Bacci et al., 2013, 2011a; Jeddizahed and Rostami, 2016; Muller et al., 2009; Oh et al., 2013; Ott et al., 2014, 2011; Ott et al., 2015, 2013; Peysson et al., 2014, 2011; Roels et al., 2016, 2014) and by using numerical simulations (Meng et al., 2015; Pruess, 2009; Pruess and Müller, 2009; Raza et al., 2015), that formation water dissolves in the dry injected CO_2, leading to oversaturation of the remaining salts and their precipitation

* Corresponding author at: SINTEF Industry, Postboks 4760 Torgarden, 7465 Trondheim, Norway.
E-mail addresses: andreasnicolas.berntsen@sintef.no (A. Berntsen), jelena.todorovic@sintef.no (J. Todorovic), martin.raphaug@sintef.no (M. Raphaug), malin.torsater@sintef.no (M. Torsæter), elvia.a.c.panduro@ntnu.no (E.A. Chavez Panduro), kamila.gawel@sintef.no (K. Gawel).

https://doi.org/10.1016/j.ijggc.2019.04.009
Received 27 August 2018; Received in revised form 1 February 2019; Accepted 11 April 2019
Available online 11 May 2019

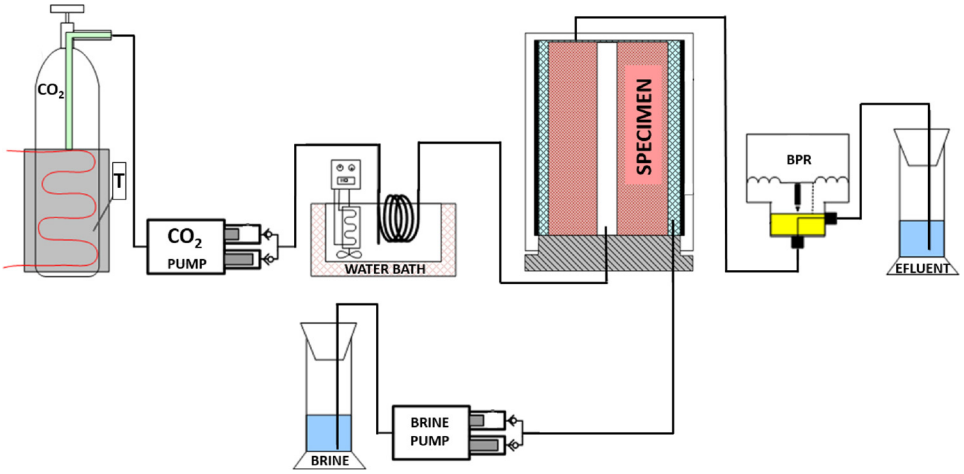

Fig. 1. A diagram of the injection setup consisting of: CO_2 bottle with riser and heating jacket; CO_2 injection pump; water bath heat exchanger; pressure cell; back pressure regulator (BPR); fluid trap for produced brine (effluent); reservoir brine pump.

inside the porous rock. Most often, axial core flooding has been done to study these phenomena experimentally, and one-dimensional models have been used in numerical simulations. The distribution of precipitate depends on among others the injection rate, the initial amount of brine, brine salinity, initial porosity and permeability as well as the phase at which CO_2 occurs (supercritical, liquid, gaseous). Depending on the conditions, salt may accumulate locally and in most cases near the injection point (Oh et al., 2013; Ott et al., 2011, 2015; Peysson et al., 2014; Roels et al., 2016), or it may be distributed evenly throughout the core (Muller et al., 2009; Ott et al., 2011, 2015; Roels et al., 2016, 2014). A reduction of absolute permeability due to salt precipitation is typically observed (Bacci et al., 2011a; Jeddizahed and Rostami, 2016; Muller et al., 2009; Ott et al., 2011, 2015; Ott et al., 2013; Peysson et al., 2014; Roels et al., 2014), but in some cases this is not considered to cause a significant CO_2 injectivity impairment (Ott et al., 2011, 2015; Ott et al., 2013; Roels et al., 2014; Van Hemert et al., 2013). A limitation of the one dimensional approach is that it includes ion diffusion and brine imbibition only in the dimension of flow; additionally, the boundaries seldom include a brine reservoir. An exception is a study by Roels et al. (Roels et al., 2016) who performed experiments flowing gaseous CO_2 through a borehole (radially outward) into a brine saturated sandstone, and investigated the effect of varying the axial length and capillary properties of the brine reservoir.

The majority of laboratory experiments on salt clogging effects described thus far in the literature have been done using boundary conditions which neglect the possibility of a continuous brine influx from the aquifer. This has been noted as a major drawback of the previously reported laboratory tests (Miri and Hellevang, 2016). Miri et al. (Miri et al., 2015) studied drying effects using microfluidic chips, and emphasized capillary brine transport along wetting films on solid grains and precipitated salt as important salt clogging mechanisms. Thus, it seems crucial for better understanding of salt clogging phenomena in the near wellbore region that experiments consider: (1) boundary conditions allowing capillary and diffusive flow and mimicking a practically infinite source of reservoir formation water and (2) a more realistic radial geometry similar to an injection well in a storage aquifer.

In this paper we present the results of an experimental approach which aimed to simulate injection of supercritical CO_2 into a highly saline sandstone storage aquifer. A hollow cylinder sandstone specimen was prepared as a downscaled model for an injection well and storage formation. Supercritical CO_2 was injected at reservoir conditions while at the outer boundary a constant supply of brine was provided at the expected rate of water evaporation. Two axial holes were drilled at some distance from the borehole and filled with cement, acting as post test indicators of CO_2 flow path due to the chemical reaction taking place between CO_2 saturated brine and cement (carbonation).

2. Materials and methods

2.1. Specimen

Bentheimer sandstone (Germany) was chosen for this study. It is a high permeability outcrop rock which is frequently used as a reservoir analogue. According to the supplier (Kocurek Industries, Texas, USA) porosity is 23–26 %, and permeability is 1500–3500 mD. The specimen was drilled with a hollow core diamond bit employing compressed air for bit cleaning and cooling. End surfaces were cut parallel to each other and perpendicular to the axis of the specimen. Final dimensions of the right hollow cylinder were 190 mm outer diameter, 50 mm hole diameter and 200 mm length. The porosity of the specimen was estimated to be 24% based on measured dimensions, mass, and the assumption that grain density equalled that of quartz (2.65 g/cm^3) (Scholz, 2010). Two holes of 4 mm diameter and 10 mm depth were drilled at 43 mm and 63 mm radii, in order to accommodate pressure gauge tubes from the top end cap. Two holes of 20 mm diameter were drilled diametrically at 60 mm radii in parallel with the axis and centre hole of the specimen, and at a 90° offset from the pressure gauge holes (illustrated in Fig. 1a in Supporting Information). These two holes extended through the specimen. The specimen was immersed in water overnight, and then the two 20 mm diameter boreholes were filled with Portland cement class G slurry (Norcem AS, Norway). The cement slurry was mixed according to API standard 10 A using local tap water (Trondheim, Norway) and 0.44 water-cement ratio. The cement hardened for three weeks. The photographs of a ready specimen are presented in Fig. 1. in Supporting Information. Right before the injection the specimen was immersed in 25 wt% NaCl brine. Gas from pore volumes was evacuated under reduced pressure. The NaCl concentration in the brine was chosen to mimic the ionic strength of the Ketzin formation (Ivanova, 2013). At experimental condition (40 °C) the brine was undersaturated in respect to NaCl (Sawamura, 2007).

2.2. CO_2 flow path indicators

The purpose of cementing two boreholes in the sandstone was to create an indicator for CO_2 flow paths. As cement typically undergoes carbonation when exposed to CO_2 saturated brines, the cement pillars were acting as indicators of the presence of CO_2 brine in the sandstone during CO_2 injection. It was expected that any potential differences in the carbonation of the indicators would contribute to better

understanding of fluids flow patterns.

2.3. CO_2 injection setup

The diagram of the injection setup is presented in Fig. 1. The specimen was mounted between a top and bottom end cap, with 1 mm thick nitrile sheets sandwiched in-between the end caps and specimen to prevent interface flow, and surrounded by a nitrile rubber sleeve of slightly larger diameter. The annulus between the specimen and sleeve was filled with high permeability proppant and functioned as an isobaric circumferential boundary. The CO_2 inlet was through a port in the centre of the bottom end cap, i.e. in the bottom of the model injection well. The outlet was through 24 flow ports in the outer periphery of the top end cap, hydraulically connected to the proppant layer. The mounted specimen was then placed inside an oil-filled high-pressure vessel which provided isometric confining stress. The entire pressure vessel was heated by an electrical heating jacket to ensure a confining oil temperature of 40 °C.

CO_2 was fed from a gas bottle via a riser tube to a high precision positive displacement syringe pump (Chandler Engineering Quizix Q5000-10 K), through a heat exchanger at 40 °C and then into the inflow port at the bottom of the specimen centre-hole. The large heat capacity of the pressure cell system ensured a constant injection temperature. The gas bottle was heated with an electrical heating jacket to increase the pressure and minimize CO_2 compression and resulting flow rate reduction during pumping. The outflow port was connected to a back pressure regulator (BPR) which was heated to prevent water freezing during rapid gas expansion. The BPR consists of a needle valve which regulates the outflow pressure. A pump (Chandler Engineering Quizix QX-6000) supplying formation brine was connected to a port in the proppant from the bottom end cap. Effluent was collected in a flask placed on a digital weight scale.

Pressure was monitored by the CO_2 injection pump, at the centre-hole of the specimen, inside the top portion of the specimen at 43 mm and 63 mm radii, at the outflow port in the top end cap, at the BPR and by the brine pump. Temperature was monitored in the pressure vessel confining oil and at the CO_2 injection pump cylinders. Effluent weight was manually recorded.

2.4. Injection procedure

Initially, a small confining pressure of 0.5 MPa was applied to ensure sealing and set the end caps against the specimen. Specimen temperature was increased from room temperature to 40 °C and left to stabilize overnight. The back pressure was supplied by pressurized nitrogen and adjusted manually, which resulted in some small drifts and subsequent corrections of the back pressure. The BPR was set to 10 MPa, so that the outflow pressure would be maintained at 10 MPa independent of flow rate, and no outflow would occur if the pore pressure was less than 10 MPa. Confining pressure was increased to 2 MPa, and formation brine was then supplied from the brine pump until the entire specimen and proppant were saturated, and the centre-hole filled. Confining pressure was increased to 20 MPa.

Injection was initiated by by-passing the injection pump and pressurizing the specimen directly from the CO_2 bottle. After pressure had equilibrated, CO_2 injection was continued by pumping at 12 ml/min, approximately 16 ml/min inside the specimen due to differences in pump and specimen temperature and resulting CO_2 density. This flow rate corresponded to approximately 0.01 mm/s radial flow velocity at the centre-hole wall if averaging the volumetric flux over the entire borehole surface. Specimen pore pressure thus increased from the gas bottle pressure (8.3 MPa) until the back pressure of 10 MPa was reached, upon which outflow commenced. Brine injection into the proppant was initiated simultaneously and was maintained at 0.016 ml/min. Maximum water saturation in supercritical CO_2 at the given thermodynamic conditions is approximately 0.1% (Spycher and Pruess, 2005) and so the brine flow rate was chosen so that ideally, water evaporation and injection remained equal, and no net water was added to the specimen. The injection continued for a net period of 6 days, with intermittent pauses due to injection pressure increases.

2.5. Methods for sample analysis

2.5.1. X-ray computed tomography (CT) and 3D visualization

After the CO_2 flooding, the specimen was scanned using X-ray computed tomography to reveal local variations in formation brine saturation and salt precipitation. Scanning was done on a medical CT scanner operating at 140 kV and variable current (typically 215–265 mA) with 1000 ms exposure time. The projections were reconstructed using the medical CT software into axial (512 × 512 pixel) and longitudinal (512 × 547 pixel) images at 0.5 mm intervals.

One of the cement pillars was cored out with a 40 mm drill bit, protected against dry-out by wrapping in plastic foil and scanned with higher resolution using an industrial CT scanner (XT H 225 ST). It was operated at 210 kV and with a current of 155 µA. The exposure time per projection was 2000 ms. A tin filter was used. The raw CT data were reconstructed into cross sectional slices (2000 × 2000 pixels), and about 2000 slices were obtained per dataset. The purpose of this additional scanning was to analyse the extent of carbonation along the cement pillars.

3D visualization of the reconstructed CT data was performed in Avizo Fire software (version 9.1, FEI, 2016).

2.5.2. X-ray powder diffraction (XRD) measurements and data analysis

Two specimens for XRD were prepared from the top and bottom portion of the tested sandstone, and one reference specimen was prepared from untested material, by first drying the samples at 50 °C and then grinding them by hand using a mortar and pestle. The measurements were performed at room temperature, between 10 and 75° 2θ on a Bruker D8 Advance DaVinci diffractometer with Bragg-Brentano geometry using CuK_α radiation ($\lambda = 1.54187$ Å). The X-ray powder diffraction pattern was collected over the course of two hours.

X-ray powder-diffraction data were refined with the Rietveld program JANA 2006 (Petříček et al., 2014). For Quantitative phase analysis (QPA) the following crystalline phase models were investigated: quartz (Wei, 1935), kaolinite (Bish and Von Dreele, 1989), halite (NaCl) (King, 1978), anatase (Weirich et al., 2000), microcline (Brown and Bailey, 1964). Background, pseudo-Voight peak shape parameters of each phase as well as phase contents were refined. Atomic positions and isotropic displacement parameters of individual atoms were refined only for quartz and fixed at values extracted from the models for other phases used in the refinement. Table 1 shows the resulting mineral quantification. Diffraction patterns are shown in Fig. 2 in The Supporting Information. The mineralogical compositions of a reference Bentheimer core, and cores drilled from the top and the bottom regions of the Bentheimer sandstone used for CO_2 injection, are presented in Table 1. For comparative quantitative NaCl content analysis the assumption was made that quartz content is homogeneous within the sample as well as it is not affected by CO_2 injection.

Table 1
The mineralogical compositions of samples from untested Bentheimer sandstone (reference) and the top and bottom of the specimen subjected to injection with standard deviations (in brackets).

Mineral	Reference	Top	Bottom
Quartz	0.980 (± 0.001)	0.987 (± 0.002)	0.970 (± 0.002)
Kaolinite	0.011 (± 0.007)	0.005 (± 0.001)	0.007 (± 0.001)
Microcline	0.007 (± 0.001)	0.001 (± 0.001)	0.002 (± 0.002)
Anatase	0.0020 (± 0.0002)	0.001 (± 0.002)	0.001 (± 0.003)
Halite (NaCl)	0	0.0060 (± 0.0003)	0.0200 (± 0.0007)

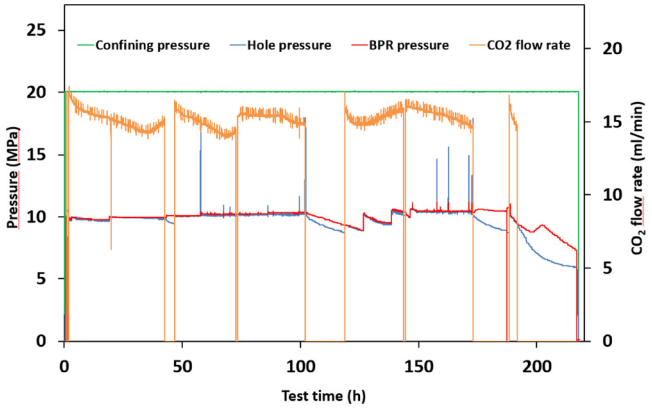

Fig. 2. Evolution of pressure with time during the experiment.

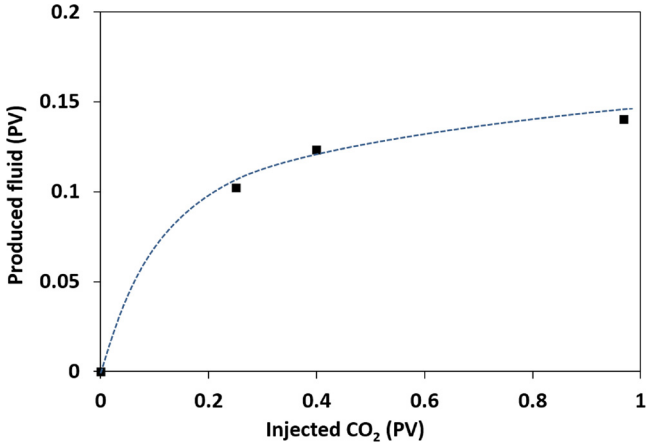

Fig. 3. Accumulated volume of the produced brine versus volume of the injected CO_2 (black squares, the blue line shows trend).

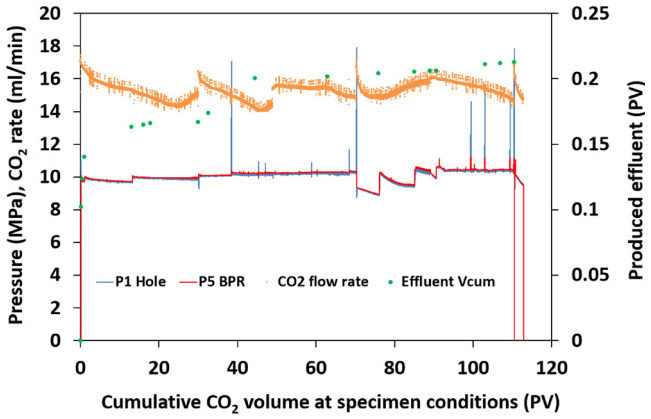

Fig. 4. Evolution of pressure and produced brine with cumulative CO_2 volume during the experiment.

2.5.3. Scanning electron microscopy

After CT scanning, the cement pillar core was prepared for scanning electron microscopy (SEM) characterization. First, three thin cross-sections (up to 10 mm thick) were cut out: from the top end, middle and bottom end (˜2.5 cm from the bottom). For each of these cross-sections, a region of interest at the cement-sandstone interface was selected, and then this section (diameter of 20 mm) was drilled out and polished. Finally, thin polished slices were imbedded in epoxy and coated with thin gold layer (10–30 nm) prior to loading in SEM.

Hitachi TM3000 TableTop SEM equipped with energy dispersive X-ray spectroscopy (EDX) was used to characterize cement-sandstone interface for the extracted samples. Backscattered electron (BSE) images were taken at 5 kV.

3. Results

3.1. Injection

A total of 110 pore volumes (PV) CO_2 was injected over a course of 9 days, including some pauses in the injection due to maintenance issues, giving a net injection time of 6 days. Fig. 2 shows the pressure evolution with time during the entire test. Confining pressure was constant at 20 MPa throughout the test, providing a large margin for any pore pressure increase due to salt clogging. Although the CO_2 pump rate was 12 ml/min, the calculated flow rate of CO_2 through the specimen varied between 14 and 17 ml/min due to variation of the difference in pump and specimen temperature. In addition to a short, temporary flow reduction at 19 h, five pauses in injection can be identified from the figure. CO_2 bottles were changed at 42 h and 73 h, and a short maintenance pause was included at 144 h. Injection was halted automatically at 102 h and 173 h due to excessive pore pressure build up, approaching the confining pressure. The pore pressure equals the back pressure while there is steady flow, but gradually reduces somewhat during periods of flow pause indicating a small leak which was estimated at 40 ml/h based on the volume needed to reach the back pressure upon reinitiating injection. No differences were observed between the pressures in the centre-hole, in the two embedded positions in the rock, nor in the top or bottom proppant layer. For simplicity, only the pressure in the centre hole is showed, representing the pore pressure in the entire specimen.

The mass of produced brine was measured at certain times during the experiment, and this is presented in Fig. 3. During the initial 0.25 PV of injected CO_2, 0.1 PV of brine was produced in a more or less steady manner as observed at the outlet. Thereafter, brine production was more intermittent and in smaller bursts. After 1 PV of injected CO_2, only 0.14 PV of brine had been produced, indicating that the initial viscous displacement of brine by CO_2 constituted only a small fraction of the total pore volume before a preferential pathway had been established. Production after this point was very limited; only 0.21 PV brine was produced in total after 110 PV of injected CO_2. Fig. 4 shows the evolution of the pressure and volume of the produced brine with respect to injected volume of CO_2. It is seen that increases in cumulative produced brine occur following pressure build-up (due to clogging) and subsequent release – notably the event at 38 h, while periods of steady flow correspond to low brine production rate. In addition to produced brine replaced from the system, water in the form of vapour most likely was released. The water vapour was not collected during the experiment; however the maximum mass of water expected to be released from the system along with CO_2 was calculated to be around 0.11 PV. The calculations are made based on assumption that the CO_2 leaving the system is saturated with water and that the solubility of water in supercritical CO_2 at the 40 °C and 10 MPa is ˜0.0011 m^3 H_2O/m^3 CO_2. (Spycher and Pruess, 2005) As the solubility of water in CO_2 decreases with decreased pressure (down to ˜$9*10^{-5}$ m^3 H_2O/m^3 CO_2 at 4 MPa (Spycher and Pruess, 2005)) it is likely that large amount of water present in CO_2 could have condensated at the outlet where the gasses expand. Nevertheless, Bacci et.al. showed that the amount of water that can exit the flooding system (T˜45 °C, p = 8 MPa) in the form of vapour can be as high as 50% of the weight of the liquid state water. (Bacci et al., 2011b)

3.2. Post-injection analysis of the specimen

After 9 days of injection the specimen was removed from the CO_2 injection cell. There was extensive, visible salt precipitate on the bottommost 4–5 cm of the center hole surface (see Fig.SI3 in The

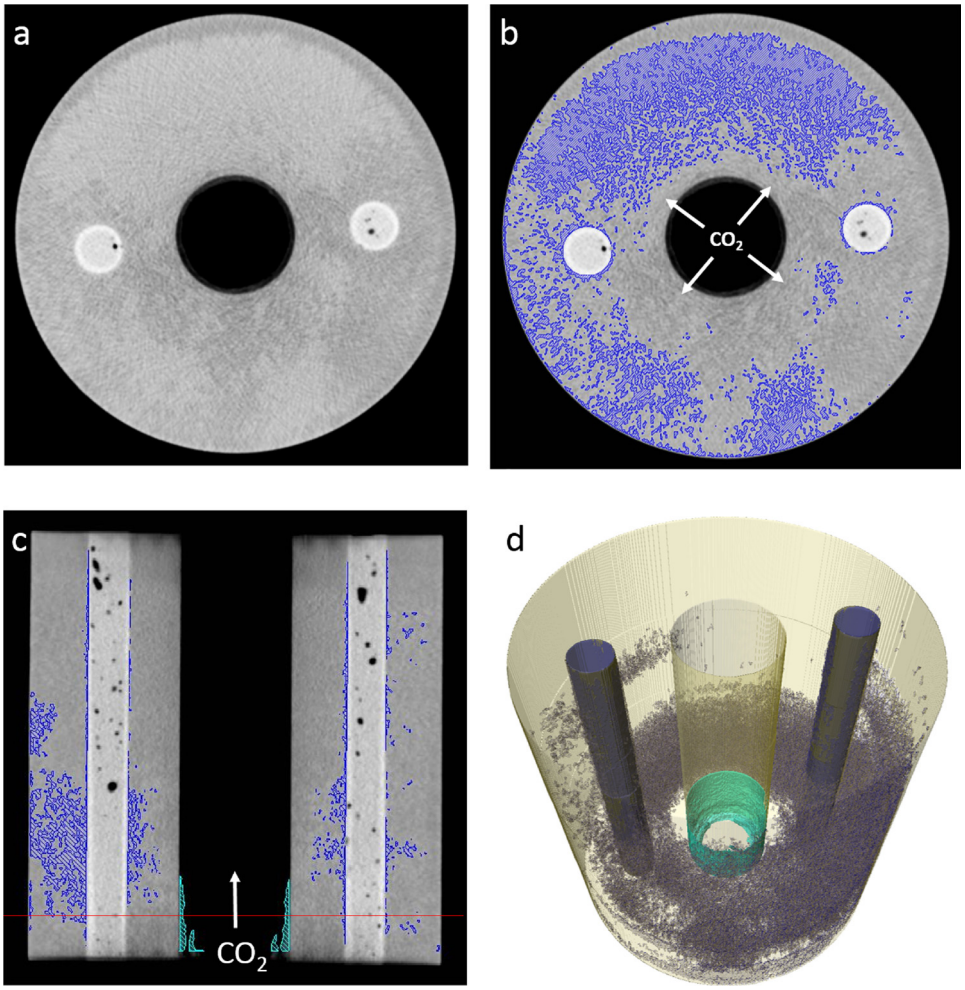

Fig. 5. CT images presenting horizontal (a and b) and vertical (c) cross-sections through the specimen exposed to supercritical CO_2 flow for 9 days. The regions of increased X-ray absorption are highlighted in blue in Fig. b. The red line on the vertical cross-section indicates the position of the horizontal cross-section. (d) The 3D representation of the specimen with highlighted salt precipitate inside the centre-hole (green) and inside the sandstone (dark blue).

Supporting Information). The specimen was protected against evaporation and then subjected to CT scanning. Representative horizontal and vertical CT cross-sections through the specimen are presented in Fig. 5. The two cement pillars are clearly visible.

The bright rim in the cement at the interface with the sandstone indicates increased X-ray absorption in this region. The effect of increased X-ray absorption is visible in the cement near the cement-sandstone interface along the whole length of the specimen (see Fig. 5a,b). We assume that the origin of this effect is increased material density and/or increase of average atomic number in the cement matrix near the interface with the sandstone due to calcium carbonate precipitation in the cement pore matrix. This will be discussed in more detail later in this section.

Regions with the highest X-ray absorption inside the sandstone matrix are highlighted in blue in Fig. 5b and c. They occupy mainly the bottom half of the specimen (see 3D visualization in Fig. 5d). The resolution of the CT images was not sufficient to distinguish between the brine and the salt at the pore scale, hence the discussion will be based on interpretation of the variation of the image intensity on cm-scale. The density of halite (2.17 g/cm^3) (John Kotz and Townsend, 2009) is sligtly lower than the density of quartz (2.65 g/cm^3)(Scholz, 2010) – the main component of Bentheimer sandstone. Nevertheless, it is expected that when sandstone pores (low density volumes) are filled with halite the brightness of regions where pores are filled with NaCl will be higher compared to the regions where pore volumes are filled with brine only. Thus the regions with the highest brightnes (i.e. X-ray absorption) are assumed to originate from increased salt content within the porous sandstone matrix which could have been due to either higher brine saturation or salt precipitation. In order to determine which of these two causes is dominant, a quantitative analysis of water and NaCl content within the porous rock matrix in the Bentheimer sandstone core was performed.

The average water content in the topmost and bottommost regions of the specimen (3 cm from the top and 3 cm from the bottom) was estimated based on gravimetric analysis of cored segments before and after complete drying. The total content of halite in the topmost and the bottommost regions was estimated based on the powder XRD measurements (described in "Materials and Methods" section). The estimated values of pore volume filled with water as well as total content of NaCl per 100 g quartz in the topmost and the bottommost regions are given in Table 2. The bottommost region contained more than twice as much water as the topmost region. The bottommost pore volume was only in 35.5% filled with brine. The partial only saturation is a result of gravity drainage of the specimen after the experimental cell was emptied from fluids. Moreover capilary forces might have to some extent redistributed the brine in the specimen. Thus the water saturation values during the experiment might have differed from the values estimated based on the post-test analysis. Nevertheless the post-test analysis of water and salt content gives a good indication of differences between the processess undergoing within the top and the bottom part of the specimen.

It was found that the topmost region contains slightly

Table 2
Average content of water and NaCl in top and bottom sides of Bentheimer sandstone after 9 days of CO_2 injection.

	TOP	BOTTOM
Pore volume filled with water/brine [%]*	15.4	35.4
Volume of water per 100 g quartz [cm^3]	1.85	4.22
Mass of NaCl per 100 g quartz [g]**	0.63	2.01
Mass of NaCl dissolved in pore water per 100 g quartz at 40 °C [g]***	0.63 (25.4 wt%)	1.56 (27 wt%)
Mass of precipitated NaCl per 100 g quartz at 40 °C [g]***	0	0.45

* Estimated based on dried out mass.
** Estimated based on semi quantitative XRD data analysis.
*** Assumed solubility 37 g NaCl/100 g H_2O at 40 °C.

undersaturated NaCl solution. The concentration of this solution was the same (within the limits of experimental error) as the concentration of brine supplied to the system before the injection onset, namely 25–26 wt%. The bottommost region contained more than three times more of NaCl than the topmost region. The amount of salt dissolved in brine and salt precipitated within the porous matrix at the experimental conditions were calculated. When the measured total concentration of salt per pore water volume exceeded NaCl solubility limit at 40 °C i.e. 37 g per 100 g of water (Sawamura et al., 2007), the excessive amount of salt was assumed to be precipitated salt. The amount of salt in the bottommost region was higher than NaCl solubility limit at experimental conditions could allow for. This suggests that beside the salt saturated brine (27 wt%) there is also a significant amount of precipitated salt in the Bentheimer pore spaces. The estimated amount of the precipitated salt was 0.45 g (m_{NaCl}) per 100 g quartz (m_Q). Given quartz density $\rho_q = 2.65\ g/cm^3$ (Scholz, 2010), NaCl density $\rho_{NaCl} = 2.17\ g/cm^3$ (John Kotz and Townsend, 2009) and sandstone porosity of 24 vol%, the sandstone pore volume fraction filled with salt (φ_{filled}) in the bottommost region was estimated to be around 1.7% based on Eq. (1):

$$\phi_{filled} = \frac{V_{NaCl/100g\ Q}}{V_{pores/100g\ Q}} \times 100\ \% = \frac{0.76 m_{NaCl/100gQ} \times \rho_Q}{0.24 m_Q \times \rho_{NaCl}} \times 100\% \quad (1)$$

where $V_{NaCl/100g\ Q}$ is volume of NaCl per 100 g of quartz, and $V_{pores/100g\ Q}$ – is volume of pores per 100 g of quartz.

The quantitative analysis of brine and precipitated salt content indicates that the higher X-ray absorption within the bottom region of the sandstone specimen results from both higher content of brine as well as a higher amount of precipitated salt in the pore volume compared to the top region.

Fig. 6 shows vertical cross sections of one of the cement pillars (pillar on the right in Fig. 5b). The altered layer was thicker at the bottom region of the pillar compared to the top (see Fig. 6b). The thickness of this layer varied also with respect to the brine and CO_2 flow directions. Surprisingly, it was the thickest at the side facing brine injection (wall with proppant – brine conduit) and thinnest at the side facing CO_2 injection port (towards the centre-hole). Fig. 6c shows the relationship between the thickness of the altered layer in the thinnest (left) and thickest (right) cross-section, and the distance from the bottom of the cement pillar i.e. sandstone specimen. The thickness of the altered layer at the very top of the specimen was around 0.3 mm. The thickness gradually increased towards the bottom. It reached approximately 1.8 mm and 3.5 mm at the sides facing CO_2 and brine injection respectively. The alteration of the cement within the topmost 5 cm was the least extensive. This slight alteration at the topside coincides with the significantly lower content of brine in the pore volume in this region.

SEM analyses of the cross-section through the sandstone/cement interface from the top, middle and bottom of the specimen were performed. For simplicity, only SEM images of the interface in the middle and bottom part of the specimen are presented in Fig. 7. More precisely, backscattered electron (BSE) images are presented, where the brightness is proportional to the average atomic number (similarly to the intensity of CT images), so they can be easily compared with the CT images. In Fig. 7a typical for cement carbonation, a brighter rim within the cement (Chavez Panduro et al., 2017; Kutchko et al., 2007) close to the cement/sandstone interface can be seen. The presence of the rim corresponds to the brighter rim within the cement pillars observed in the CT images (Fig. 5). This brighter zone within the cement observed by the two techniques is referred to in literature as carbonated zone. (Kutchko et al., 2007) The brightness contrast between the carbonated and unreacted zones is a result of density difference between carbonation product i.e. calcium carbonate (d = 2.71 g/ml) and substrate i.e. calcium hydroxide (d = 2.21 g/ml). The 1.5 mm thick carbonated zone is indicated in Fig. 7a by a red arrow. The SEM image captured for the bottom (˜2,5 cm height) cross-section shows a 200–300 µm thick zone with higher porosity (darker spots) than the cement bulk present within the carbonated zone close to the cement/sandstone interface, (see Fig. 7b). This higher porosity is an effect of calcium carbonate dissolution.(Carroll et al., 2016; Kutchko et al., 2007, 2008) The dissolution is due to a reaction of acid with calcium carbonate which leads to the formation of water soluble calcium bicarbonate ($Ca^{2+} + 2HCO_3^-$) and thus leaching of calcium carbonate from the cement matrix if convective transport is present (which is the case in the bottom region of specimen). The calcium depleted porous zone was not observed in the top and middle cross-section samples where the carbonation front was not that advanced and where the carbonated zone was narrower.

4. Discussion

During the course of the experiment, no significant pressure build-up was observed across the rock specimen, indicating that permeable flow paths were not completely clogged. Darcy's law applied to the cylindrical geometry and assuming perfectly radial flow is of the form $\Delta p = Q\mu \ln(r_e/r_i)/2\pi kL$. The pressure difference resulting from a flow of 16 ml/min is of the order of 10 Pa, much lower than the resolution of the pressure transducers (˜500 Pa). Thus, partial clogging of flow paths could occur without being indicated by changes in differential pressure measurements. Low content of brine in the topmost region indicates that brine from this region has been displaced. Due to buoyancy (Cardoso and Andres, 2014), the CO_2 injected at the bottom of the centre hole will tend to penetrate into the uppermost parts of sandstone cylinder on its way to the outlet. Strong gravity segregation is expected to occur over relatively short time-scales because of the large density differences between the resident brine ($1.19\ g/cm^3$) and the injected supercritical CO_2 ($0.63\ g/cm^3$). (Møll Nilsen et al., 2011; Span and Wagner, 1996) Thus at the beginning of CO_2 injection displacement of brine from the topmost regions mostly occurred due to CO_2 buoyancy and viscous displacement between the pumped CO_2 and the brine. Around 300 ml of brine was expelled from the system during the first hour of injection. This volume corresponds to approximately 14% of the total pore volume of the specimen. This suggests that around one fifth of the topmost pore space might have been utilized as a CO_2 flow path. During the later stages of the injection, viscous brine displacement was negligible and evaporation was the main water displacement mechanism from the system. Precipitation of salt was most pronounced close to the CO_2 inlet, suggesting that drying was most efficient in the region where the dry CO_2 was in contact with the brine. Salt precipitate was observed both at the surface of the centre hole and in the rock pores mainly at the bottom side of the specimen. This suggests that the largest evaporative fluxes occur nearest to the injection point where supercritical CO_2 is not yet saturated with water vapour. The local decrease of water saturation close to the injection point can to some extent be compensated by capillary backflow of formation water towards the well (Miri and Hellevang, 2016). This could explain why the bottommost region of the specimen was still rich in brine despite of extensive

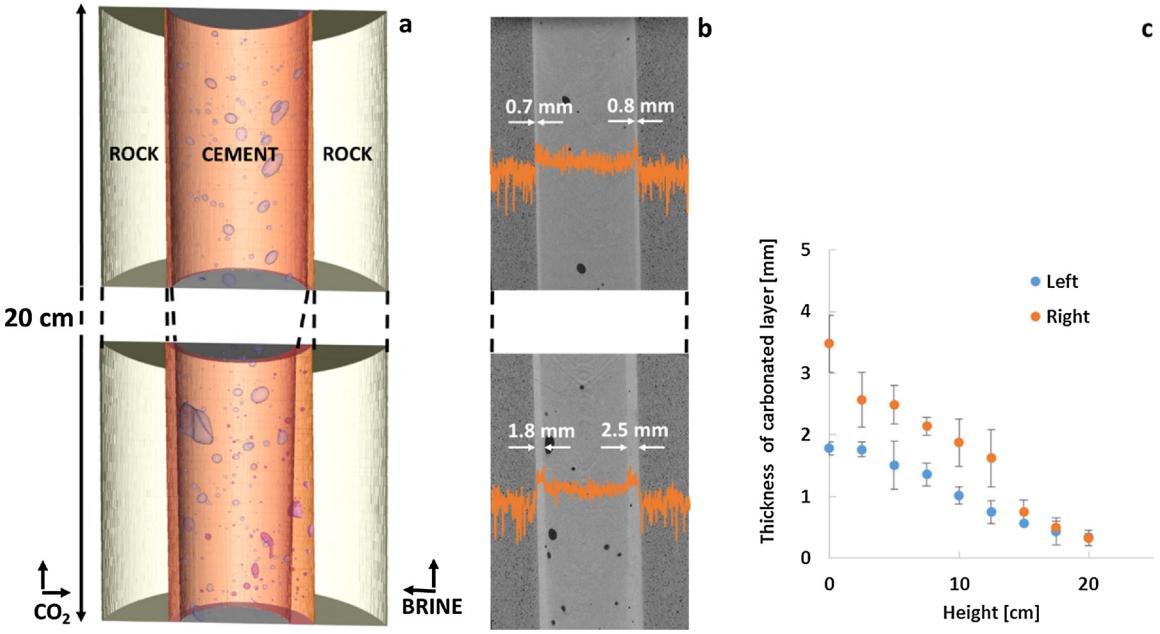

Fig. 6. Cross-sections through the rock with cement pillar towards the top (˜5 cm) and bottom (˜5 cm) of the specimen (width not to scale with height): (a) 3D representation, orange – carbonated zone, grey centre – intact cement, violet - voids, (b) Vertical CT cross-sections with intensity profiles. (c) Thickness of the carbonated layer vs. height for inward (facing CO_2 inlet at the left side) and outward (facing brine inlet at the right side) cross-sections. Each point is an average of three measurements. The error bars represent standard deviation from the mean value.

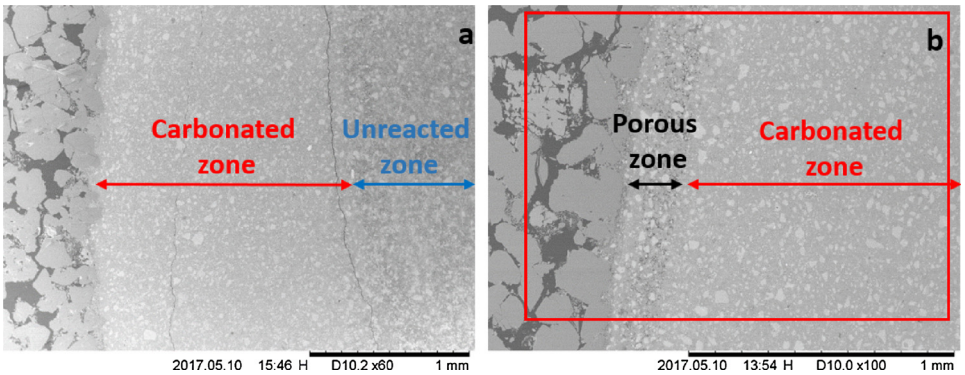

Fig. 7. SEM (BSE) image of the cross-section through the rock/cement interface taken from the middle (at ˜10 cm hight)(a) and bottom (at ˜2.5 cm hight) (b) section of the specimen. The arrows indicate unreacted (blue), carbonated (red) and porous dissolution zone (black).

precipitation. The absence of salt precipitate and the presence of slightly undersaturated brine (25.4 wt%) in the topmost region suggests that CO_2 that flowed through this region was already entirely saturated with water and thus did not cause any further drying in this region. Based on these observations, the residence time was likely much longer than the time needed for complete water saturation. The theoretical upper bound on the CO_2 residence time in the cell is 100 min, but the actual residence time is probably significantly less and scales inversely with the flow path volume which is difficult to quantify.

Fig. 8 depicts the proposed flow patterns of brine and dry and wet CO_2 within the downscaled near wellbore reservoir model as well as the most likely drying regimes in different regions. Miri et al. distinguish between three main drying regimes and their resulting distribution of salt precipitate (Miri and Hellevang, 2016):

(1) The *diffusive regime* occurs at very low injection rates when evaporation is slow enough to allow sufficient diffusion of salts away from the evaporation interface, preventing local oversaturation and precipitation. Precipitation under this regime will be spatially quite homogeneous.
(2) The *capillary regime* occurs when the rate of evaporation is high, water losses are compensated by capillary brine backflow, and diffusion of ions away from the interface is too slow to prevent oversaturation. This causes massive salt accumulation at the drying front.
(3) The *evaporative regime* exists at high injection rates when the rate of evaporation is higher than the rate of capillary backflow. Salt precipitation in this regime will result in rather homogeneous deposition of salt within the dried out porous medium.

The post-injection CT analysis of salt distribution within the specimen combined with water content analysis suggests that there might have been two different drying regimes acting within our specimen. The presence of the accumulated salt precipitation in the bottommost regions of the centre hole walls coinciding with high water content in this region suggest the capillary precipitation regime. In this region significant evaporative flux must have been compensated by the capillary backflow of brine. On the other hand, right above the bottommost region with visible salt precipitate in the centre hole there is a region with homogeneous salt distribution within the sandstone pore spaces. The most probable drying regime in this region is the diffusive one where the evaporative flux is low compared to the capillary flux. The lower

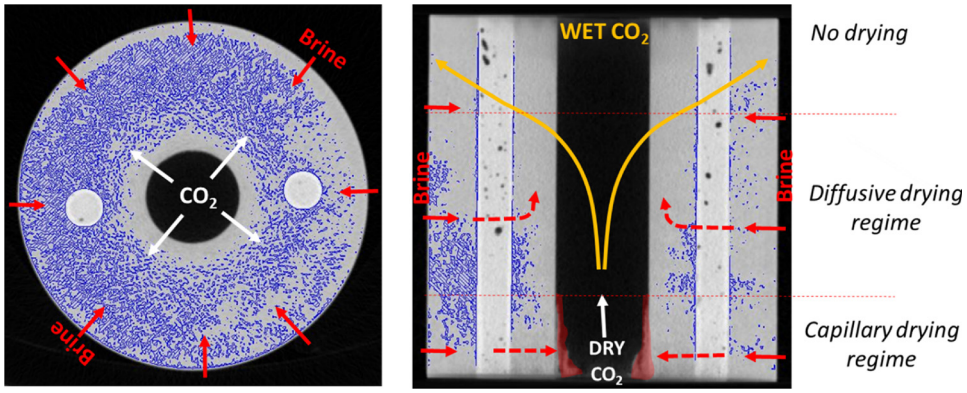

Fig. 8. The results underline the importance of understanding possible drying and salt precipitation issues prior to drilling, to ensure that optimal completion solutions can be chosen (Monteiro et al. (2017)).

evaporative flux in this region is most likely associated with higher humidity of the CO_2 flowing in this region due to partial water saturation in the bottommost area. Apparently, the injection rate applied here was too low to allow for the evaporative regime to occur. Due to long CO_2 residence time the CO_2 flowing through the topmost regions was already water saturated thus did not cause any drying in this region.

The typical Portland well cement is susceptible to carbonation when exposed to carbonated brine, but it is resistant to dry CO_2 (Carroll et al., 2016; Chavez Panduro et al., 2017; Duguid, 2009; Duguid et al., 2011; Duguid and Scherer, 2010; Kutchko et al., 2007, 2008; Matteo and Scherer, 2012; Riaz et al., 2006; Walsh et al., 2013). The degree of carbonation of the cemented pillars is an indication of availability of carbonated brine. Carbonated brine reacts with portlandite ($Ca(OH)_2$) and calcium silicate hydrate (C-S-H phase) present in the hardened cement. These reactions lead to the formation of poorly water-soluble calcium carbonate ($CaCO_3$) in the cement matrix. This primary carbonation process often results in a decrease in overall cement porosity and permeability (Bachu and Bennion, 2009) which was manifested by an increased X-ray absorption within the cement close to the sandstone/cement interface in the CT data (see Figs. 5a,b and 6). The carbonation has been confirmed by SEM analysis. The SEM imaging showed also cement degradation due to calcium carbonate dissolution in the bottommost sections of cement pillars. The cement degradation that follows carbonation is a process caused by transformation of the poorly water-soluble calcium carbonate to easily soluble calcium bicarbonate at low pH conditions. This results in leaching out of the cementitous material which leads to cement degradation. The faster the carbonation and carbonate dissolution processes are, the broader dissolution zone is expected (Kutchko et al., 2007; Walsh et al., 2013). A small degree of carbonation of the cement pillars was observed within the topmost region (5 cm long) compared to the bottommost region. The rate of cement carbonation depends on availability of reactive CO_2 species like carbonate and bicarbonate ions (CO_3^{2-}, HCO_3-) in the cement matrix (Brunet et al., 2016). This availability is related to thermodynamic conditions (temperature and partial CO_2 pressure) and to reactants transport capabilities within the surrounding media (Brunet et al., 2016; Walsh et al., 2013). The less extensive carbonation in the topmost region may be a result of either (1) lower concentration of carbonate and bicarbonate ions (CO_3^{2-}, HCO_3-) in the brine in this region or (2) a limited transport of carbonate ions to the cement surface within this region compared to the bottommost region. The limited transport could have been a result of significantly lower brine content in the pore matrix in the topmost region.(Genty and Pot, 2014; Ghanbarian et al., 2014) This low brine saturation within the upper part of the sandstone could have been a likely cause of constrained diffusive and convective transport of carbonate and bicarbonate ions (CO_3^{2-}, HCO_3-) to the cement surface resulting in a limited carbonation compared to the middle and bottommost region.(Genty and Pot, 2014; Ghanbarian et al., 2014)

On the other hand, the concentration of these ions might have been higher in the bottommost region due to density differences between the brine and CO_2-rich brine (Cardoso and Andres, 2014; Riaz et al., 2006). Once CO_2 dissolves in brine, the mixture becomes denser. Due to density differences between CO_2 free and CO_2 rich brine the interface between these two fluids may become gravitationally unstable. This will lead to the formation of so-called fingers that transport the CO_2-rich brine downward, while deeper, CO_2 free, formation water will rise. Convection is much faster transport mechanism than molecular diffusion (Pau et al., 2010) and a convective mixing establishes within minutes to hours timescale.(Faisal et al., 2015; MacMinn and Juanes, 2013) This process may have caused an uneven distribution of carbonate ions along the specimen length, namely higher concentration of these ions in the bottommost region and thus more extensive carbonation. In addition, in the capillary drying regime in the bottommost region the transport is supported by capillary forces that drag water towards the dried-out regions. The more extensive carbonation at the sides facing brine inlet compared to centre hole sides at the bottom must have been due to higher availability of carbonate ions on this side. The reason why the carbonate ions where more available on the brine inlet side can be twofold: (1) they were constantly supplied along with the brine transported by capillary forces and/or (2) their concentration was higher at lower salt concentrations present closer to brine inlet then inside the specimen where brine was losing water and getting saturated.

5. Implications for carbon storage projects

The medium scale CO_2 injection experiments presented here mimic supercritical CO_2 injection into a saline aquifer where the salinity of reservoir waters is high and close to the saturation at the reservoir conditions. Although no significant pressure build-up was observed across the rock specimen, during the course of the injection, salt precipitation within the borehole of the wellbore model as well as in the porous rock matrix occurred. This may suggest that wellbore and reservoir clogging may undergo without early stage pressure build-up symptoms which may delay identification of salt clogging problem and decisions about remediation operations until the situation becomes critical. Clogging of the entire borehole diameter or CO_2 flow pathways within the rock that could lead to complete CO_2 flow path blockage seems likely but would require longer exposure to dry CO_2. Given that after 9 days of injection 46% of the borehole radius closest to the CO_2 inlet was filled with halite and assuming a linear decrease of the borehole radius with time upon salt precipitation we have estimated that the complete closure of the borehole diameter at given experimental conditions may occur after around 20 days. A typical production casing is around 2.8 times larger thus the time needed to close the hole

would be around 56 days at similar temperature, pressure and flow rate conditions. The above estimation is, however, very rough and calls for a detailed study of salt precipitation kinetics in the borehole system.

We have shown that in the wellbore and near wellbore region different drying regimes can be expected on a relatively short length scale. The type of drying regime will be related to the distance from the injection point. Its occurrence and range will depend on CO_2 residence time and water saturation thus will be directly related with flow rate and drying kinetics at certain reservoir conditions.

In the present experimental campaign only one injection geometry was tested, which corresponds to open hole completion of a CO_2 injection well. It can, however, be expected that the choice of well completion (open hole or cased hole with perforations) may affect injection geometry and thus also fluid distribution within the near wellbore region and salt precipitation regimes. It would therefore be valuable to validate experimentally how different completion strategies affect CO_2 injectivity.

The results suggest also that carbonation of a cement sheath present within the reservoir section in the case of a cased hole completion, will depend on the distribution of fluids within the reservoir. The accumulation of CO_2-rich brines at the bottom of the reservoir will result in a higher concentration of carbonate ions in these regions and thus enhanced carbonation of the well cement placed at the bottom of the reservoir section. On the other hand, in the regions from which brine is displaced i.e. close to the caprock the carbonation will be less significant than in the regions rich in CO_2 saturated brines. The drying effect can thus be positive for the integrity of the well as it has a potential to slow down the carbonation processes.

6. Conclusions

This paper reports medium-scale experiments on salt precipitation in the near-wellbore region upon a dry CO_2 injection. The uniqueness of the experimental approach applied in this work relies on (1) realistic radial geometry of CO_2 flow similar to wellbore geometry, and (2) opened boundary conditions for brine inflow allowing capillary and diffusive flux of brine components from and to practically infinite source of reservoir formation water. The experiment involved injection of supercritical CO_2 (40 °C and 100 bar) into a thick-wall sandstone cylinder representing a downscaled near-wellbore region over a period of nine days. During the course of injection, no significant pressure build-up was observed across the rock specimen, indicating that permeable flow paths were not entirely clogged. Partial clogging of the model wellbore took place close to the CO_2 inlet but also salt precipitated in the rock matrix in the near wellbore region. Post-test analysis of the specimen and the incorporated CO_2 indicators provided indication of the most probable flow patterns of supercritical CO_2 and CO_2 rich brines in the system. We have shown that in the wellbore and near wellbore region different drying regimes can be expected on a relatively short length interval. At our experimental conditions, three different drying regimes were found to occur in different wellbore regions. Simultaneous occurrence of these different regimes was ascribed to the differences in water saturation of the CO_2 passing by the different regions. The results underline the importance of understanding possible drying and salt precipitation issues prior to drilling, to ensure that optimal completion solutions can be chosen.

Acknowledgements

The authors gratefully acknowledge financial support from the research project "Avoiding loss of CO_2 injectivity" (255490/E20) which was funded by The Research Council of Norway through the CLIMIT program. Work done by E. A. Chavez Panduro (XRD characterisation) was financed by the project "Closing the gaps in CO_2 well plugging" (243765/E20) which was also funded by The Research Council of Norway through the CLIMIT program. Special thanks go to Bartlomiej Gawel for semi-quantitative XRD data analysis. We also thank NTNU Department of Physics and NTNU NanoLab (NorFab) for using their laboratories and equipment. The Research Council of Norway is acknowledged for the support to the Norwegian Micro- and Nano-Fabrication Facility, NorFab.

Appendix A. Supplementary data

Supplementary material related to this article can be found, in the online version, at doi:https://doi.org/10.1016/j.ijggc.2019.04.009.

References

Bacci, G., Korre, A., Durucan, S., 2011a. An experimental and numerical investigation into the impact of dissolution/precipitation mechanisms on CO2 injectivity in the wellbore and far field regions. Int. J. Greenh. Gas Control. 5, 579–588.
Bacci, G., Korre, A., Durucan, S., 2011b. Experimental investigation into salt precipitation during CO2 injection in saline aquifers. Energy Procedia 4, 4450–4456.
Bacci, G., Durucan, S., Korre, A., 2013. Experimental and numerical study of the effects of halite scaling on injectivity and seal performance during CO2 injection in saline aquifers. Energy Procedia 3275–3282.
Bachu, S., Bennion, D.B., 2009. Experimental assessment of brine and/or CO2 leakage through well cements at reservoir conditions. Int. J. Greenh. Gas Control. 3, 494–501.
Baumann, G., Henninges, J., De Lucia, M., 2014. Monitoring of saturation changes and salt precipitation during CO2 injection using pulsed neutron-gamma logging at the Ketzin pilot site. Int. J. Greenh. Gas Control. 28, 134–146.
Bish, D.L., Von Dreele, R.B., 1989. Rietveld refinement of non-hydrogen atomic positions in kaolinite. Clays Clay Miner. 37, 289–296.
Brown, B.E., Bailey, S.W., 1964. The structure of maximum microcline. Acta Crystallogr. 17, 1391–1400.
Brunet, J.-P.L., Li, L., Karpyn, Z.T., Huerta, N.J., 2016. Fracture opening or self-sealing: critical residence time as a unifying parameter for cement–CO2–brine interactions. Int. J. Greenh. Gas Control. 47, 25–37.
Cardoso, S.S.S., Andres, J.T.H., 2014. Geochemistry of silicate-rich rocks can curtail spreading of carbon dioxide in subsurface aquifers. Nat. Commun. 5, 5743.
Carroll, S., Carey, J.W., Dzombak, D., Huerta, N.J., Li, L., Richard, T., Um, W., Walsh, S.D.C., Zhang, L., 2016. Review: role of chemistry, mechanics, and transport on well integrity in CO2 storage environments. Int. J. Greenh. Gas Control. 49, 149–160.
Chavez Panduro, E.A., Torsæter, M., Gawel, K., Bjørge, R., Gibaud, A., Yang, Y., Bruns, S., Zheng, Y., Sørensen, H.O., Breiby, D.W., 2017. In-situ X-ray tomography study of cement exposed to CO < inf > 2 < /inf > Saturated brine. Environ. Sci. Technol. 51, 9344–9351.
Duguid, A., 2009. An estimate of the time to degrade the cement sheath in a well exposed to carbonated brine. Energy Procedia 3181–3188 1 ed.
Duguid, A., Scherer, G.W., 2010. Degradation of oilwell cement due to exposure to carbonated brine. Int. J. Greenh. Gas Control. 4, 546–560.
Duguid, A., Radonjic, M., Scherer, G.W., 2011. Degradation of cement at the reservoir/cement interface from exposure to carbonated brine. Int. J. Greenh. Gas Control. 5, 1413–1428.
Eiken, O., Ringrose, P., Hermanrud, C., Nazarian, B., Torp, T.A., Høier, L., 2011. Lessons learned from 14 years of CCS operations: sleipner, in Salah and snøhvit. Energy Procedia 5541–5548.
Faisal, T.F., Chevalier, S., Bernabe, Y., Juanes, R., Sassi, M., 2015. Quantitative and qualitative study of density driven CO2 mass transfer in a vertical Hele-Shaw cell. Int. J. Heat Mass Transf. 81, 901–914.
Genty, A., Pot, V., 2014. Numerical calculation of effective diffusion in unsaturated porous media by the TRT lattice boltzmann method. Transp. Porous Media 105, 391–410.
Ghanbarian, B., Daigle, H., Hunt, A., Ewing, R.P., Sahimi, M., 2014. Gas and Solute Diffusion in Partially Saturated Porous Media: Percolation Theory and Effective-medium Approximation Compared with Lattice-boltzmann Simulations.
Grude, S., Landrø, M., Dvorkin, J., 2014. Pressure effects caused by CO2 injection in the Tubåen Fm., the Snøhvit field. Int. J. Greenh. Gas Control. 27, 178–187.
Hansen, O., Gilding, D., Nazarian, B., Osdal, B., Ringrose, P., Kristoffersen, J.-B., Eiken, O., Hansen, H., 2013. Snøhvit: the history of injecting and storing 1 Mt CO2 in the fluvial tubåen Fm. Energy Procedia 37, 3565–3573.
Ivanova, A., 2013. Geological Structure and Time-Lapse Studies of CO2 Injection at the Ketzin Pilot Site, Germany. Doctoral thesis. Uppsala University, Disciplinary Domain of Science and Technology, Earth Sciences, Department of Earth Sciences, Geophysics.
Jeddizahed, J., Rostami, B., 2016. Experimental investigation of injectivity alteration due to salt precipitation during CO < inf > 2 < /inf > sequestration in saline aquifers. Adv. Water Resour. 96, 23–33.
John Kotz, P.T., Townsend, John, 2009. Chemistry and Chemical Reactivity.
King, L.W.F.H., 1978. A revised method of operation of the single-crystal diamond cell and refinement of the structure of NaCl at 32 kbar. Am. Mineral. 63, 337–342.
Kutchko, B.G., Strazisar, B.R., Dzombak, D.A., Lowry, G.V., Thauiow, N., 2007. Degradation of well cement by CO2 under geologic sequestration conditions. Environ. Sci. Technol. 41, 4787–4792.
Kutchko, B.G., Strazisar, B.R., Lowry, G.V., Dzombak, D.A., Thaulow, N., 2008. Rate of CO < inf > 2 < /inf > attack on hydrated class H well cement under geologic sequestration conditions. Environ. Sci. Technol. 42, 6237–6242.

MacMinn, C.W., Juanes, R., 2013. Buoyant currents arrested by convective dissolution. Geophys. Res. Lett. 40, 2017–2022.
Martens, S., Möller, F., Streibel, M., Liebscher, A., 2014. Completion of five years of safe CO < inf > 2 < /inf > injection and transition to the post-closure phase at the Ketzin pilot site. Energy Procedia 190–197.
Matteo, E.N., Scherer, G.W., 2012. Experimental study of the diffusion-controlled acid degradation of Class H Portland cement. Int. J. Greenh. Gas Control. 7, 181–191.
Meng, Q., Jiang, X., Li, D., Xie, Q., 2015. Numerical simulations of pressure buildup and salt precipitation during carbon dioxide storage in saline aquifers. Comput. Fluids 121, 92–101.
Miri, R., Hellevang, H., 2016. Salt precipitation during CO < inf > 2 < /inf > storage-a review. Int. J. Greenh. Gas Control. 51, 136–147.
Miri, R., van Noort, R., Aagaard, P., Hellevang, H., 2015. New insights on the physics of salt precipitation during injection of CO2 into saline aquifers. Int. J. Greenh. Gas Control. 43, 10–21.
Møll Nilsen, H., Herrera, P.A., Ashraf, M., Ligaarden, I., Iding, M., Hermanrud, C., Lie, K.-A., Nordbotten, J.M., Dahle, H.K., Keilegavlen, E., 2011. Field-case simulation of CO2 -plume migration using vertical-equilibrium models. Energy Procedia 4, 3801–3808.
Monteiro, A.O., Loredo, A., Costa, P.M.F.J., Oeser, M., Cachim, P.B., 2017. A pressure-sensitive carbon black cement composite for traffic monitoring. Constr. Build. Mater. 154, 1079–1086.
Morozova, D., Zettlitzer, M., Let, D., Würdemann, H., 2011. Monitoring of the microbial community composition in deep subsurface saline aquifers during CO < inf > 2 < / inf > storage in Ketzin, Germany. Energy Procedia 4362–4370.
Muller, N., Qi, R., Mackie, E., Pruess, K., Blunt, M.J., 2009. CO2 injection impairment due to halite precipitation. Energy Procedia 3507–3514 1 ed.
Oh, J., Kim, K.Y., Han, W.S., Kim, T., Kim, J.C., Park, E., 2013. Experimental and numerical study on supercritical CO < inf > 2 < /inf > /brine transport in a fractured rock: implications of mass transfer, capillary pressure and storage capacity. Adv. Water Resour. 62, 442–453.
Ott, H., De Kloe, K.D., Marcelis, F., Makurat, A., 2011. Injection of supercritical CO < inf > 2 < /inf > in brine saturated sandstone: pattern formation during salt precipitation. Energy Procedia 4425–4432.
Ott, H., Snippe, J., De Kloe, K., Husain, H., Abri, A., 2013. Salt precipitation due to sc-gas injection: single versus multi-porosity rocks. Energy Procedia 3319–3330.
Ott, H., Andrew, M., Snippe, J., Blunt, M.J., 2014. Microscale solute transport and precipitation in complex rock during drying. Geophys. Res. Lett. 41, 8369–8376.
Ott, H., Roels, S.M., de Kloe, K., 2015. Salt precipitation due to supercritical gas injection: I. Capillary-driven flow in unimodal sandstone. Int. J. Greenh. Gas Control. 43, 247–255.
Pau, G.S.H., Bell, J.B., Pruess, K., Almgren, A.S., Lijewski, M.J., Zhang, K., 2010. High-resolution simulation and characterization of density-driven flow in CO2 storage in saline aquifers. Adv. Water Resour. 33, 443–455.
Petříček, V., Dušek, M., Palatinus, L., 2014. Crystallographic Computing System JANA2006: General Features, Zeitschrift Für Kristallographie - Crystalline Materials. p. 345. .
Peysson, Y., Fleury, M., Blázquez-Pascual, V., 2011. Drying rate measurements in convection- and diffusion-driven conditions on a shaly sandstone using nuclear magnetic resonance. Transp. Porous Media 90, 1001–1016.
Peysson, Y., André, L., Azaroual, M., 2014. Well injectivity during CO < inf > 2 < / inf > storage operations in deep saline aquifers-Part 1: experimental investigation of drying effects, salt precipitation and capillary forces. Int. J. Greenh. Gas Control. 22, 291–300.
Pruess, K., 2009. Formation dry-out from co2 injection into saline aquifers: 2. Analytical model for salt precipitation. Water Resour. Res. 45.
Pruess, K., Müller, N., 2009. Formation dry-out from co2 injection into saline aquifers: 1. Effects of solids precipitation and their mitigation. Water Resour. Res. 45.
Raza, A., Rezaee, R., Gholami, R., Rasouli, V., Bing, C.H., Nagarajan, R., Hamid, M.A., 2015. Injectivity and quantification of capillary trapping for CO&inf&2&/inf& storage: a review of influencing parameters. J. Nat. Gas Sci. Eng. 26, 510–517.
Riaz, A., Hesse, M., Tchelepi, H.A., Orr, F.M., 2006. Onset of convection in a gravitationally unstable diffusive boundary layer in porous media. J. Fluid Mech. 548, 87–111.
Roels, S.M., Ott, H., Zitha, P.L.J., 2014. μ-CT analysis and numerical simulation of drying effects of CO2 injection into brine-saturated porous media. Int. J. Greenh. Gas Control. 27, 146–154.
Roels, S.M., El Chatib, N., Nicolaides, C., Zitha, P.L.J., 2016. Capillary-driven transport of dissolved salt to the drying zone during CO < inf > 2 < /inf > Injection in homogeneous and layered porous media. Transp. Porous Media 111, 411–424.
Sawamura, S., 2007. High-pressure investigations of solubility. Pure Appl. Chem. 79, 861–874.
Sawamura, S., Egoshi, N., Setoguchi, Y., Matsuo, H., 2007. Solubility of sodium chloride in water under high pressure. Fluid Phase Equilib. 254, 158–162.
Scholz, F., 2010. Electroanalytical Methods: Guide to Experiments and Applications.
Span, R., Wagner, W., 1996. A new equation of state for carbon dioxide covering the fluid region from the triple-point temperature to 1100 K at pressures up to 800 MPa. J. Phys. Chem. Ref. Data 25, 1509–1596.
Spycher, N., Pruess, K., 2005. CO2-H2O mixtures in the geological sequestration of CO2. II. Partitioning in chloride brines at 12–100°C and up to 600 bar. Geochim. Cosmochim. Acta 69, 3309–3320.
Van Hemert, P., Rudolph, E.S.J., Zitha, P.L.J., 2013. Micro computer tomography study of potassium iodide precipitation in bentheimer sandstone caused by flow-through CO2 drying. Energy Procedia 3331–3346.
Walsh, S.D.C., Du Frane, W.L., Mason, H.E., Carroll, S.A., 2013. Permeability of wellbore-cement fractures following degradation by carbonated brine. Rock Mech. Rock Eng. 46, 455–464.
Wei, P.H., 1935. Die Bindung im Quarz Zeitschrift fuer Kristallographie. Kristallgeometrie, Kristallphysik, Kristallchemie 92, 355–362.
Weirich, T.E., Winterer, M., Seifried, S., Hahn, H., Fuess, H., 2000. Rietveld analysis of electron powder diffraction data from nanocrystalline anatase TiO2. Ultramicroscopy 81, 263–270.
Zettlitzer, M., Moeller, F., Morozova, D., Lokay, P., Würdemann, H., 2010. Re-establishment of the proper injectivity of the CO2-injection well Ktzi 201 in Ketzin, Germany. Int. J. Greenh. Gas Control. 4, 952–959.